nature neuroscience

Hippocampal CA1 pyramidal cells form functionally distinct sublayers

Kenji Mizuseki[1], Kamran Diba[1,2], Eva Pastalkova[1,2] & György Buzsáki[1]

Hippocampal CA1 pyramidal neurons have frequently been regarded as a homogeneous cell population in biophysical, pharmacological and modeling studies. We found robust differences between pyramidal neurons residing in the deep and superficial CA1 sublayers in rats. Compared with their superficial peers, deep pyramidal cells fired at higher rates, burst more frequently, were more likely to have place fields and were more strongly modulated by slow oscillations of sleep. Both deep and superficial pyramidal cells fired preferentially at the trough of theta oscillations during maze exploration, whereas deep pyramidal cells shifted their preferred phase of firing to the peak of theta during rapid eye movement (REM) sleep. Furthermore, although the majority of REM theta phase-shifting cells fired at the ascending phase of gamma oscillations during waking, nonshifting cells preferred the trough. Thus, CA1 pyramidal cells in adjacent sublayers can address their targets jointly or differentially, depending on brain states.

Although the molecular, anatomical and functional diversity of cortical interneurons is well documented[1–3], principal cells are typically grouped together on the basis of their cortical layer and/or subregion assignments. However, several recent observations have suggested that there are distinct subgroups of principal neurons with different properties, projections and local interactions, even in the same region and cortical layer[4–14]. In the neocortex and entorhinal cortex, specialized subnetworks of excitatory neurons have been described in[8–10] and across cortical layers[12,13]. These subnetworks may assist in segregating different streams of information[4,10,14].

The hippocampal CA1 region is a model system that is frequently used to study plasticity, pharmacological effects and intracellular features. In the rodent, CA1 pyramidal neurons form a compact layer consisting of 5–8 superimposed rows of pyramidal neurons. Each pyramidal cell is typically assumed to have similar morphology, inputs, outputs and biophysical properties[15]. In contrast with this notion, anatomical experiments indicate that the medial and lateral entorhinal cortex project preferentially to proximal and distal parts of the CA1 region[16], respectively. Correlated with this topography, pyramidal cells show a gradually increasing propensity of emitting spike bursts[17] and decreasing spatial specificity in the proximo-distal (CA3 to subiculum) direction[18]. Other physiological observations also point to functional segregation in CA1 pyramidal cells. For example, the magnitude of somatodendritic backpropagation of action potential shows a bimodality, perhaps as a result of subtle morphological differences of pyramidal cells[19]. The phase preference of CA1 pyramidal cells to gamma oscillations also has a bimodal distribution[20].

Another potential source of variability of CA1 pyramidal neurons is the position or depth relative to the cell layer[21]. Supporting this hypothesis, early studies have demonstrated segregation of calbindin immunoreactivity[22] and zinc content[23] in the deep and superficial substrata of CA1 pyramidal layer, and, more recently, within-layer differences have become apparent in gene expression studies[24,25]. However, functional differences between deep and superficial CA1 pyramidal neurons are not known, and most physiological experiments and modeling studies have assumed that pyramidal neurons in the CA1 sublayers are homogeneous. Exploiting the capability of silicon probes to localize the relative vertical position of neuronal somata in the recorded volume of neuronal tissue[26], we examined the functional properties of the superficial and deep CA1 pyramidal cells in the behaving rat. We found two subcircuits that were differentially controlled by intra- and extra-hippocampal inputs and could distinctly affect their targets in a brain state–dependent manner.

RESULTS

Local field potentials (LFPs) and unit firing were recorded in the hippocampal CA1 pyramidal layer (n = 10 rats; **Fig. 1**). In four of the rats, recordings were made simultaneously in CA1 and in multiple layers of the medial entorhinal cortex[27]. Recordings were carried out while the rat ran on an open field (180 cm by 180 cm, or 120 cm by 120 cm), a linear track (250 cm long), an elevated plus maze (100 cm by 100 cm) or a zigzag maze (100 cm by 200 cm), or performed a T-maze alternation task or a rewarded wheel-running task[27] (hereafter, theta periods during behavioral tasks are referred to as RUN). Recordings were also carried out during sleep, typically both before and after tasks, in the animal's home cage.

Localization of neuronal somata in the CA1 pyramidal layer

The vertical span (140 µm) and the precise distribution of the eight recording sites on the probe shanks (20-µm vertical steps) allowed us to determine the relative depths of the cell bodies of the simultaneously recorded neurons (**Fig. 1a–c**). The site with the largest spike

[1]Center for Molecular and Behavioral Neuroscience, Rutgers, The State University of New Jersey, Newark, New Jersey, USA. [2]Present address: Janelia Farm Research Campus, Howard Hughes Medical Institute, Ashburn, Virginia, USA (E.P.), Department of Psychology, University of Wisconsin at Milwaukee, Milwaukee, Wisconsin, USA (K.D.). Correspondence should be addressed to G.B. (buzsaki@axon.rutgers.edu).

Received 11 February; accepted 30 June; published online 7 August 2011; doi:10.1038/nn.2894

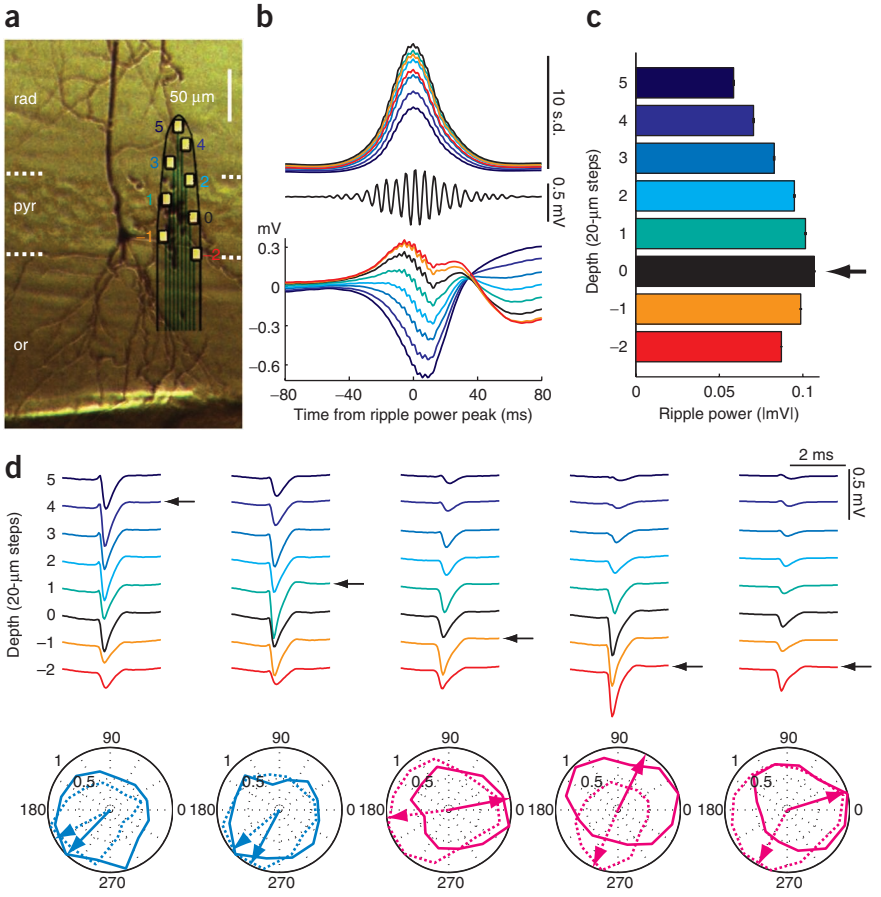

Figure 1 Spatial localization of neuronal somata in the CA1 pyramidal layer. (**a**) Biocytin-filled neuron in the deep CA1 pyramidal cell layer. Surrounding unstained neuronal somata provide reference for the recording sites of the superposed silicon probe. Recording sites (–2 to 5) are color coded. 0 designates the middle of the layer, determined by the maximum ripple power (black in **b**–**d**). rad, stratum radiatum; pyr, stratum pyramidale; or, stratum oriens. (**b**–**d**) Data from a shank from a single session. (**b**) Middle, filtered (140–230 Hz) single trace at depth 0. Bottom, average LFP traces triggered by ripple power peaks (n = 2,635), recorded at different depths. Top, mean integrated ripple power at different depths, normalized by the s.d. of ripple power at depth 0. Color code refers to recording sites in **a**. (**c**) Ripple power at different recording depths (mean ± s.e.m., **b**, top). The recording site with the largest ripple power identifies the middle of the pyramidal layer (arrow, reference depth 0) and serves for the determination of the distance of the recorded cell body of individual neurons from the middle of the layer. (**d**) Average waveforms of five simultaneously recorded neurons (1 Hz to 5 kHz). Arrows indicate the putative position of the neuron's soma relative to the reference depth, inferred from the largest spike amplitude[26]. Two superficial neurons (that is, above reference depth 0) and three deep neurons (below reference depth 0) are shown. Polar plots of spike phase distribution of the five neurons referenced to the theta oscillation in the CA1 pyramidal layer (peak of theta = 0°, 360°; trough = 180°). Normalized contour plots and preferred spike phase of the neurons (arrows) during maze running (dotted) and REM sleep (solid). Magenta polar plots represent REM-shifting neurons and light blue plots nonshifting cells. Positive polarity is up in all figures.

amplitude for each unit was regarded as the location of the cell body[26] (**Fig. 1d**). The site with the largest amplitude of ripples, reflecting the middle of the pyramidal layer[28] (designated as site 0; **Fig. 1a**–**c**), was also determined for each shank (**Fig. 1c**) and served as the reference depth for calculating the distance of the cell bodies from the middle of the pyramidal layer.

Although the stratum oriens is stereotaxically above the pyramidal layer in the dorsal CA1 region of the rodent hippocampus, we use the traditional terminology of cortical anatomy, in which deep and superficial refer to the direction of the basal and apical dendrites, respectively[29]. For reliably separating neurons according to depth, the neurons with the largest action potentials at site 0 were termed middle, and those above (close to stratum radiatum) and below (close to stratum oriens) recording site 0 were termed superficial and deep, respectively. The middle layer likely contained a mixture of deep and superficial neurons and served as a separator between the 'true' deep and superficial cells. These three tentative divisions contained approximately equal numbers of recorded neurons (deep, 1,228; middle, 1,204; superficial, 1,109). Somata above site 3 and below site –3 were rare (<8.5%) and were therefore lumped together with the somata recorded at sites 3 and –3, respectively.

Shifting theta phase preference between waking and REM

Five well-isolated[30] pyramidal neurons from a single shank were spatially distributed along the vertical (oriens-radiatum) axis (**Fig. 1d**). During maze exploration, all five of the neurons fired preferentially near the trough (180°) of the LFP theta recorded in the pyramidal layer. During REM sleep, the two superficial neurons continued to discharge near the trough, whereas the three neurons in the deeper parts of the layer shifted their preferred firing phase by almost half a theta cycle[31]. To quantify this observation across sessions and rats, we determined the phase preference of each significantly theta phase–modulated pyramidal neuron during both exploration and REM sleep (see Online Methods). The preferred theta phase of neurons during REM sleep varied with depth ($P < 0.0001$, circular ANOVA), with deep neurons showing a preference for the peak of the theta waves, as shown by the significantly different mean theta phase preference of neurons at deeper sites (**Fig. 2a**; for individual rats, see **Supplementary Fig. 1**). To simplify further analysis, we grouped neurons recorded at different depths into superficial, middle and deep subgroups. During REM sleep, the phase preference distributions across subgroups were significantly different ($P < 0.0001$, Watson U^2 test; **Fig. 2b**; for individual rats, see **Supplementary Fig. 1**) but were similar during RUN. In the deep sublayer, approximately half of the pyramidal cells fired preferentially near the peak of theta during REM sleep.

Given that theta peak–preferring cells during REM may themselves comprise a functionally separate group that does not segregate perfectly in depth (**Fig. 2b**), we also separately compared the properties of REM phase–shifting and nonshifting cells, exploiting the bimodal distribution of phase preferences during REM (**Fig. 2b**,**c**). Pyramidal cells that were significantly phase-locked ($P < 0.01$, Rayleigh test, see Online Methods) to theta oscillations during REM sleep (68.3%, 1,937 of 2,838 CA1 pyramidal neurons that fired at least 50 spikes during REM) were broadly divided into REM-shifting (<120° or >300°

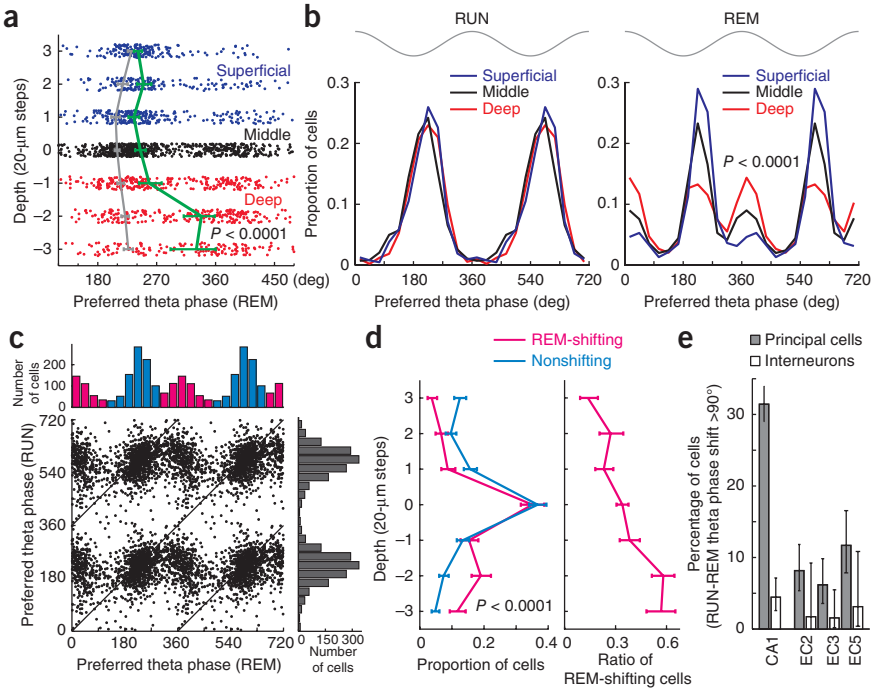

Figure 2 Preferred theta phase of spikes during REM sleep depends on the position of the soma in the CA1 pyramidal layer. (**a**) Preferred theta phase for each neuron (dots) recorded at different depths of the layer during REM sleep. Solid lines indicate mean (±95% confidence intervals) preferred theta phase (green, REM). For comparison, the mean preferred theta phase during RUN (gray) is also shown. The few neurons above and below recording sites 3 and −3 were added to values at 3 and −3, respectively. (**b**) Distribution of the preferred theta phase of pyramidal cells in the superficial (recording sites above 0), middle (site 0) and deep (sites below 0) depths during maze running (RUN) and REM sleep. Note the unimodal distribution of theta phase preference in the deep layer group during RUN and bimodal distribution during REM sleep. Top gray traces indicate idealized reference theta cycle in CA1 pyramidal layer. (**c**) Distribution of preferred theta phases during RUN and REM sleep. Only neurons that showed significant theta-phase modulation during both RUN and REM sleep are included here. Top and right, theta phase preference histograms for REM sleep and RUN. Note the bimodal distribution of preferred theta phase during REM sleep. Neurons with <120° or >300° preferred theta phases during REM (magenta) were designated as REM-shifting cells, whereas those between 120° to 300° (blue) were designated as nonshifting cells. (**d**) Left, depth distribution of REM-shifting and nonshifting neurons (±95% Clopper-Pearson confidence intervals). Right, distribution of the fraction of REM-shifting cells as a function of depth in the pyramidal layer. (**e**) Percent of neurons with >90° phase shift between RUN and REM (±95% Clopper-Pearson confidence intervals) in different regions. EC2, EC3 and EC5 correspond to neurons in layers II, III and V of the entorhinal cortex, respectively. Interneurons did not shift phase preference across states. Theta phase of LFP recorded from the CA1 pyramidal cell layer was used for all of the cell types.

preferred theta phases during REM) and nonshifting groups (120° to 300° preferred theta phases; **Fig. 2c**). Overall, 35.1% (679 cells) belonged to the REM-shifting category. As expected, the depth distributions of REM-shifting and nonshifting neurons were significantly different ($P < 0.0001$, two-sample Kolmogorov-Smirnov test, one-tail; **Fig. 2d**). The ratio of REM-shifting cells doubled from the superficial–middle sublayers to the deep sublayer (**Fig. 2d**).

To compare these observations with CA1 interneurons and with neurons in the entorhinal cortex, we calculated the fraction of these cells that shifted their preferred phase from RUN to REM by more than 90° (**Fig. 2e**). In contrast with CA1 pyramidal cells, CA1 interneurons did not shift their preferred phase between wake and REM states. Furthermore, neurons with >90° phase shift between RUN and REM in the various layers of the entorhinal cortex (EC2, EC3 and EC5) were rare (**Fig. 2e** and **Supplementary Fig. 2**). Thus, the theta phase shift of CA1 pyramidal neurons during REM sleep cannot simply be explained by altered timing from the entorhinal input (**Supplementary Figs. 2** and **3**).

Phase-locking of CA1 pyramidal cells by slow oscillations

To examine whether the CA1 sublayer–specific groups differed in other behavioral states, we examined their firing patterns during non-REM sleep. A prominent physiological feature of non-REM sleep in neocortical-paleocortical structures is the presence of slow cortical oscillations, associated with UP and DOWN states of neurons[32]. Slow oscillations also affect hippocampal network patterns[33]. To detect slow oscillations, we summed the spiking activity of all of the simultaneously recorded entorhinal cortex neurons and identified more than 150-ms silent periods, followed by more than 200 ms of activity, as DOWN-UP transitions[33] (**Fig. 3**). When segregated according to depth, neurons in superficial, middle and deep CA1 subgroups showed significantly different magnitudes of modulation by the entorhinal slow oscillation ($P < 0.0001$, $F = 22.19$, ANOVA; **Fig. 3**, results in individual rats are shown in **Supplementary Fig. 4**).

When segregated on the basis of theta-phase shift during REM sleep, neurons in the REM-shifting group, relative to the nonshifting group, showed significantly stronger phase modulation by the slow oscillation ($P < 0.0001$, t test; **Fig. 3**). Together, these findings indicate that the entorhinal input can differentially activate superficial and deep subgroups of CA1 pyramidal cells during slow-wave sleep.

We also investigated the relationship between sharp wave–ripple patterns[28] and the depth of CA1 pyramidal cells. The fraction of spikes during ripples (relative to all spikes during slow-wave sleep episodes) was not significantly different between superficial and deep neurons (superficial = 8.17 ± 5.33%, deep = 8.20 ± 4.95%, $P > 0.2$, t test, but the middle group was significantly higher than both sublayers; middle = 8.90 ± 4.93, mean ± s.d., $P < 0.01$). On the other hand, REM-shifting cells were more strongly associated with ripple activity, as evidenced by both the higher fraction of spikes during ripples (8.94 ± 4.93% versus 7.18 ± 4.12%, $P < 0.0001$, t test) and a higher percentage of ripples associated with spiking, relative to nonshifting cells (17.2 ± 12.1% versus 15.4 ± 12.8%, mean ± s.d., $P < 0.005$). These findings indicate that REM-shifting neurons respond more vigorously to CA3 inputs during sharp wave–ripples.

Firing rate, burst and activity-dependence of theta phase

Next, we examined whether CA1 pyramidal cells in the different sublayers differ in their spiking properties and how these differences might relate to their theta phase preference. Neurons in the deeper part of the pyramidal layer had significantly higher overall firing rates than did superficial neurons ($P < 0.0001$, rank sum test; **Fig. 4a** and **Supplementary Fig. 5**). In addition to rate, calculation of spike-burst

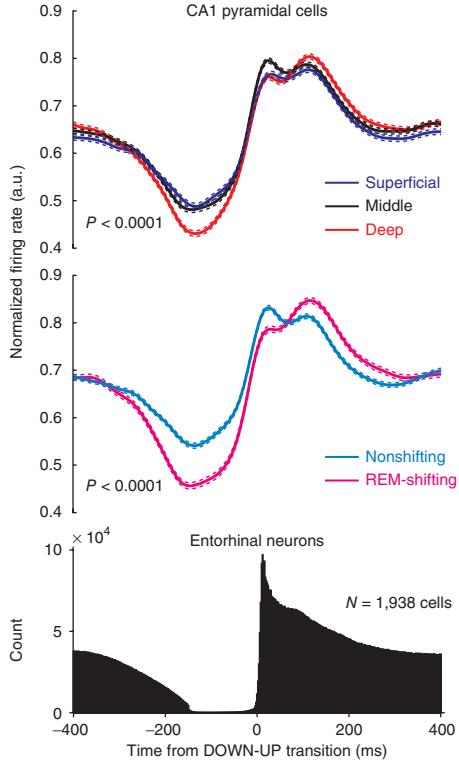

Figure 3 Phase-locking of CA1 pyramidal cell spikes by slow oscillations is location dependent. Top, peri-event firing rate histograms of CA1 pyramidal neurons in the superficial, middle and deep sublayers during slow oscillations in sleep. The firing rates of single cells were normalized by peak firing rates. Mean ± s.e.m. is shown for each group. a.u., arbitrary units. Middle, rate histograms of REM-shifting and nonshifting neurons. Bottom, entorhinal cortex unit firing histogram. Time zero is the DOWN-UP transition of slow oscillation.

index, defined as the fraction of spikes with <6-ms interspike intervals (ISIs)[27,30], revealed that superficial neurons were significantly less 'bursty' than their deeper peers ($P < 0.0001$, rank sum test; **Fig. 4b** and **Supplementary Fig. 6**).

Firing rate and burst propensities were also significantly different between REM-shifting and nonshifting cells (**Supplementary Figs. 5** and **6**). REM-shifting cells decreased their firing rates significantly more during REM sleep compared with RUN ($P < 0.0001$, *t* test; **Fig. 4c**), and were also significantly more 'bursty' during REM sleep compared with RUN ($P < 0.0001$, *t* test; **Fig. 4d**).

Because of the known correlation between discharge frequency and the theta phase of spikes[27,34,35], we examined how firing pattern changes, from single spikes to burst firing, affected the theta phase of spiking. Spikes of each neuron were sorted into eight ISI categories, and the significance of theta modulation, preferred theta phase and modulation depth were calculated for each neuron in each category[27] (**Fig. 5**, **Supplementary Fig. 7** and Online Methods). During RUN, both REM-shifting and nonshifting neurons preferred the phase near the trough, with a mostly weak dependence on the ISI. An exception was for <6-ms bursts in REM-shifting neurons, which showed a relatively wide phase preference (**Fig. 5a**,**c**). In contrast, during REM sleep, nearly all bursts of REM-shifting neurons preferred the peak of the theta cycle (<15-ms ISI groups, $P < 0.0001$, Watson-Williams test, RUN-REM comparison; **Fig. 5b** and **Supplementary Fig. 7**), whereas most single spikes (>20-ms ISIs) continued to fire after the trough. In the nonshifting group, both single spikes and bursts continued to fire after the trough during REM sleep (**Fig. 5d**).

During RUN, a large percentage of both REM-shifting and nonshifting neurons were significantly phase-modulated by theta ($P < 0.01$, Rayleigh test, see Online Methods), relatively independently of the ISIs (**Fig. 5e**). However, the percentage of significantly theta-modulated neurons was larger for both bursts (ISI < 10 ms) and single spikes (ISI > 30 ms) in the REM-shifting group than in the nonshifting cells. During REM sleep, the percentage of significantly theta-modulated neurons during bursting was significantly higher in the REM-shifting than in the nonshifting group ($P < 0.0001$, χ^2 independent test), whereas the percentage of significantly theta-modulated neurons for single spikes was significantly higher in the nonshifting group than in the REM-shifting group ($P < 0.0001$; **Fig. 5f**).

In the significantly phase-modulated groups, we also analyzed the magnitude of theta phase-modulation (mean resultant

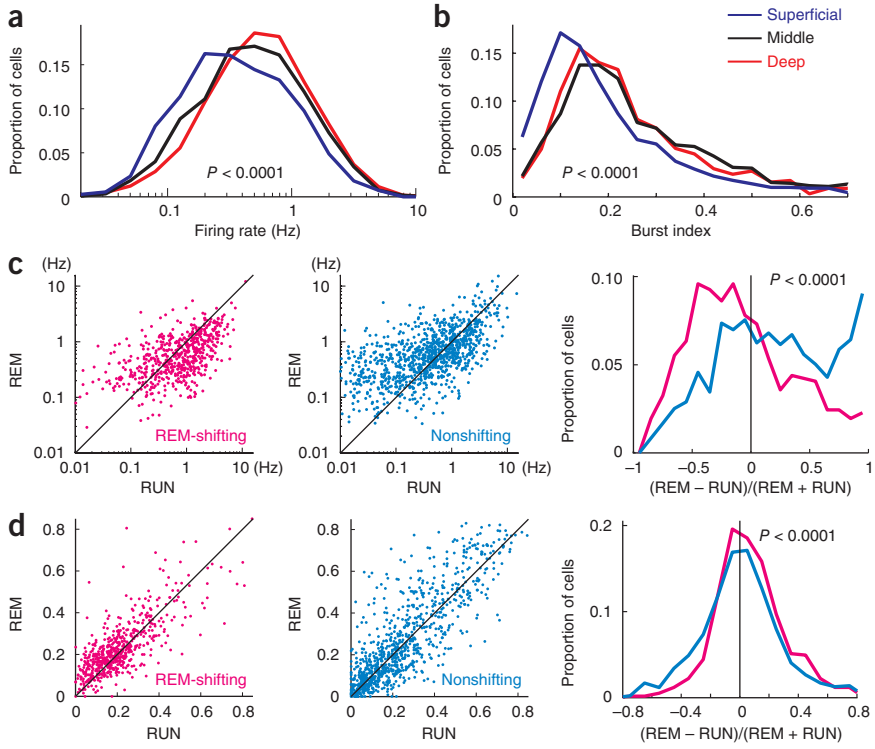

Figure 4 Firing rates and bursting properties of CA1 pyramidal cells. (**a**,**b**) Distribution of overall firing rates (Hz, log scale, **a**) and burst index (fraction of spikes with <6-ms ISIs, either preceding or following spikes, **b**) for neurons located in the superficial, middle and deep sublayers. (**c**) Firing rates of REM-shifting (left) and nonshifting neurons (middle) during maze running (RUN) and REM sleep. REM-shifting neurons were significantly less active during REM sleep than during RUN. Right, distribution of the magnitude and direction of firing rate changes across states. (**d**) Burst index of REM-shifting and nonshifting neurons during maze running (RUN) and REM sleep. REM-shifting neurons were significantly more bursty during REM sleep than during RUN.

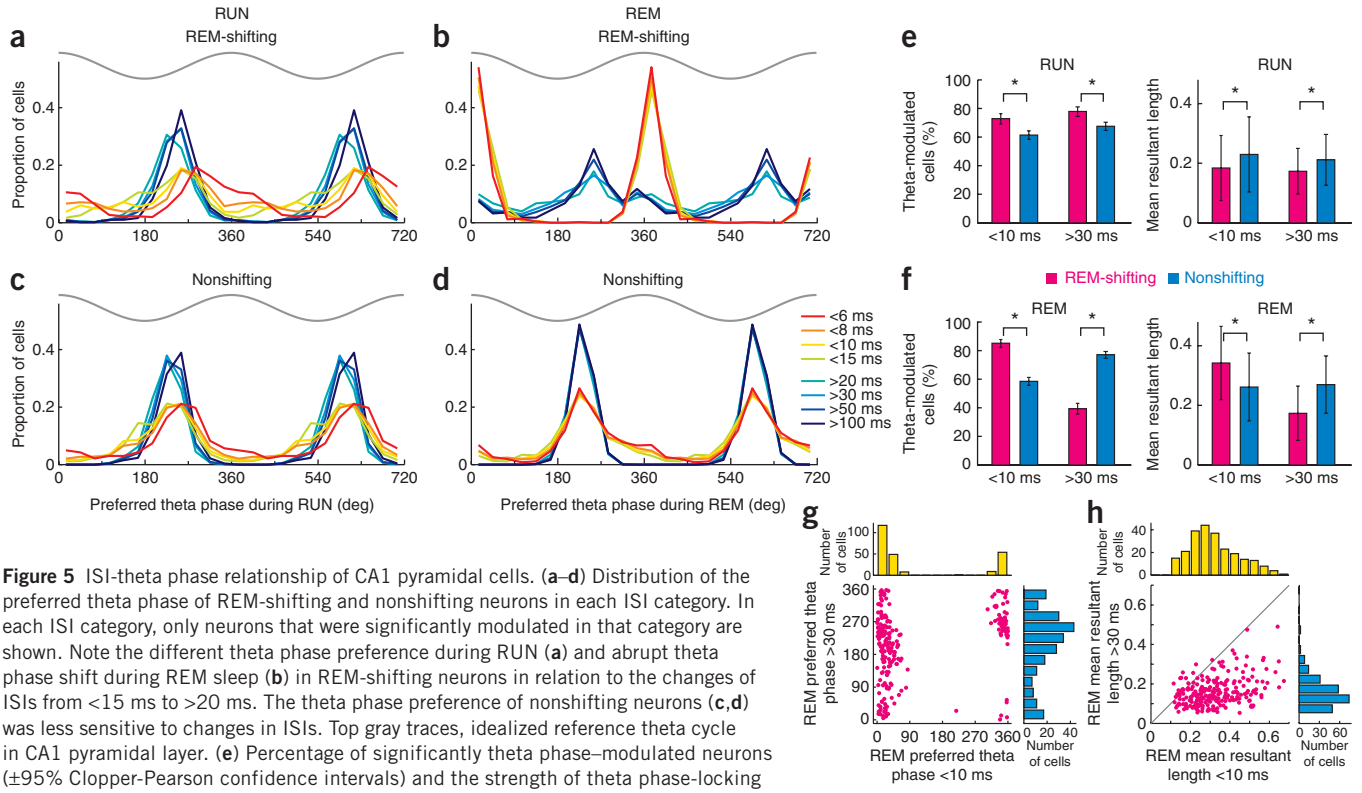

Figure 5 ISI-theta phase relationship of CA1 pyramidal cells. (**a**–**d**) Distribution of the preferred theta phase of REM-shifting and nonshifting neurons in each ISI category. In each ISI category, only neurons that were significantly modulated in that category are shown. Note the different theta phase preference during RUN (**a**) and abrupt theta phase shift during REM sleep (**b**) in REM-shifting neurons in relation to the changes of ISIs from <15 ms to >20 ms. The theta phase preference of nonshifting neurons (**c**,**d**) was less sensitive to changes in ISIs. Top gray traces, idealized reference theta cycle in CA1 pyramidal layer. (**e**) Percentage of significantly theta phase–modulated neurons (±95% Clopper-Pearson confidence intervals) and the strength of theta phase-locking (mean resultant length, mean ± s.d.) in the <10-ms and >30-ms ISI categories during RUN. REM-shifting (magenta) and nonshifting (blue) neurons are shown separately. (**f**) Data presented as in **e** for REM sleep. All comparisons between REM-shifting and nonshifting groups were significant (*$P < 0.0001$, χ^2 test for percent of modulated cells, t test for mean resultant length). (**g**) Comparison of preferred theta phase between <10-ms and >30-ms categories of the same neurons during REM sleep. Only REM-shifting cells significantly modulated for both ISI categories are shown. (**h**) Data presented as in **g** for comparison of mean resultant length.

length). Brain state change exerted a differential effect on the magnitude of theta phase-locking of spikes across the REM-shifting and nonshifting neurons (**Fig. 5e**,**f**). During RUN, nonshifting neurons were more strongly phase-locked than were REM-shifting cells, during both bursts (ISI < 10 ms) and single-spike firing (ISI > 30 ms) patterns (**Fig. 5e**). During REM, this difference remained the same for single spikes but was reversed for bursts. In fact, the theta phase-modulation of burst events (<10-ms intervals) in REM-shifting neurons was almost twice as powerful during REM as during RUN (**Fig. 5e**,**f**). Comparison of ISI groups from REM-shifting neurons revealed that the same cells shifted their preferred phase from trough (ISI > 30 ms) to peak (ISI < 10 ms) and increased their phase modulation during burst events (**Fig. 5g**,**h**).

In summary, deep and superficial neurons have different firing rates and bursting properties. During REM sleep, REM-shifting (that is, mainly deep) neurons burst more, as compared with RUN, and bursts of spikes of REM-shifting cells were more strongly modulated by theta and showed stronger theta peak preference than nonshifting neurons. Thus, the interactions among instantaneous firing rate, bursting, theta modulation and preferred theta phase depend on the joint effect of brain state and cell location in the CA1 pyramidal layer.

Higher incidence of place cells in the deep CA1 sublayer

Hippocampal neurons in rodents show location-selective firing[36]. Neurons with peak firing rates exceeding 2 Hz on the linear track or on the open field (see Online Methods) were defined as place cells[18]. The proportion of place cells was significantly higher in the deep sublayer than in the superficial layer ($P < 0.0001$, χ^2 independent test; **Fig. 6**). This was also the case when we used a spatial coherence greater than 0.7 as the criteria for defining place fields[37,38] (**Supplementary Fig. 8**).

The distributions of peak firing rates and within-field mean rates were also significantly different across the depth groups ($P < 0.0001$; **Supplementary Figs. 9** and **10**), consistent with the overall rate difference described above. Information content[39–41] (both bits per spike and bits per second) was also significantly different across the CA1 sublayers and between REM-shifting and nonshifting cells ($P < 0.01$; **Supplementary Figs. 9** and **10**), with information content per spike being higher in the superficial and nonshifting groups than in the deep and REM-shifting groups. Other examined features of place cells

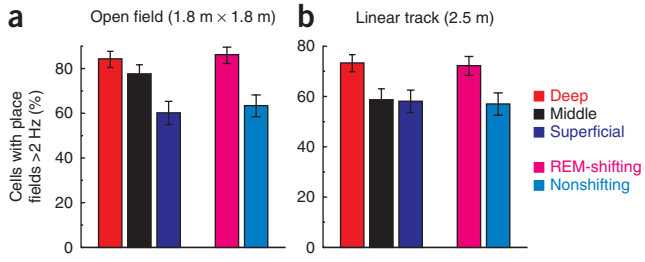

Figure 6 Larger fraction of place cells in deep layer neurons and REM-shifting group. (**a**) Proportion of neurons with place fields, defined by peak firing rate (>2 Hz, Online Methods), in different sublayers and in the REM-shifting and nonshifting groups during open field exploration. Clopper-Pearson confidence intervals ($P < 0.05$) are shown. (**b**) Data presented as in **a** for neurons recorded on the linear track (for other spatial features, see **Supplementary Figs. 8–10**).

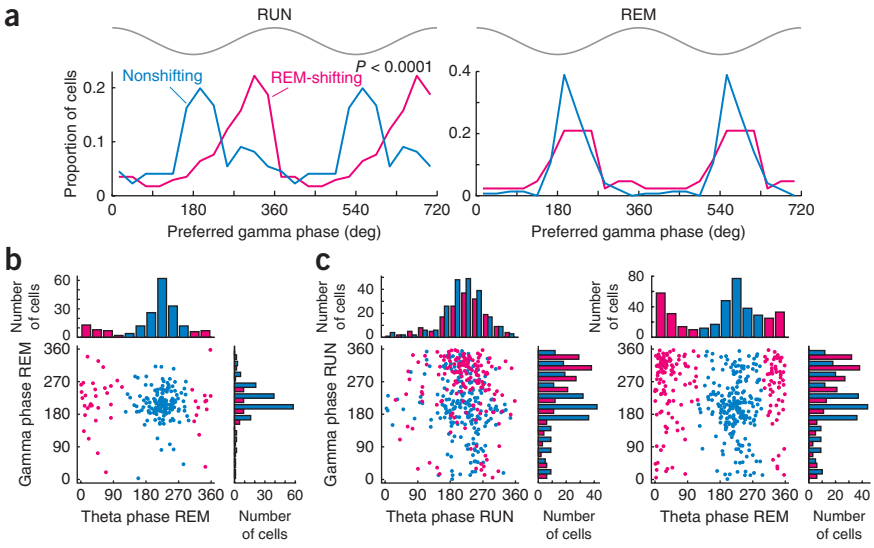

Figure 7 Relationship between theta and gamma phase preferences of CA1 pyramidal cells. (**a**) Distribution of preferred phase of gamma oscillation (30–80 Hz) during maze running (RUN) and REM sleep, shown separately for REM-shifting and nonshifting neurons. Note that both groups fired preferentially at the trough of local gamma waves (~180°) during REM sleep, whereas the majority of REM-shifting neurons were phase-locked to the rising phase (gammaR) of the gamma cycle during RUN. The reference site for LFP gamma was the middle of the pyramidal layer (site 0 in **Fig. 1**). Two gamma cycles are shown for better visibility. Top gray traces represent the idealized reference gamma cycle in CA1 pyramidal layer. (**b**,**c**) Modulation of pyramidal cells by both gamma and theta. Note that most gamma-modulated neurons during REM were nonshifting neurons (**b**, light blue) and most gammaR neurons during RUN belonged to the REM-shifting group (**c**, magenta). The side histograms in **b** and **c** (right) are the same as the plots in **a**. Only neurons that were significantly modulated by both theta and gamma oscillations are included in the plots in **b** and **c**.

(place field size, spatial coherence[37] and stability[41]) were not different across the groups (**Supplementary Figs. 9** and **10**). In addition, the slopes of phase precession[42] on the linear track were similar across depth groups (**Supplementary Fig. 10**).

Consistent with the results of the depth analysis, the proportion of place cells was significantly higher in the REM-shifting group than in the nonshifting neurons in both the linear track and the open field ($P < 0.001$, χ^2 independent test; **Fig. 6**). On the other hand, the slopes of phase precession[42] on the linear track were similar between the REM-shifting and nonshifting groups (**Supplementary Fig. 10**). In summary, although the proportion of active place cells in a given environment was higher in the deep (REM-shifting) group, the major spatial features and theta phase dynamics of place cells were not different across groups.

Relationship between theta and gamma phase preference

The hippocampus also displays prominent gamma oscillations[43–45], and it was recently found that spikes of pyramidal cells in the waking rat show phase preference to either the trough (gammaT neurons, 30–240°) or the rising phase of the gamma wave[20] (gammaR neurons, 0–30° or 240–360°). We confirmed this bimodal gamma phase distribution during RUN (**Fig. 7a**) and found that, during REM, virtually all of the significantly gamma-modulated pyramidal cells were phase-locked to the trough of gamma waves[20] (**Fig. 7a**,**b**).

The preferred gamma phase during RUN showed a depth-dependent shift, with a preference of deep cells for the rising phase of the gamma cycle (**Supplementary Fig. 11**), although this effect was less robust than the depth-dependent theta-phase preference during REM. On the other hand, the matches between gammaR and REM-shifting and between gammaT and nonshifting cells were strong (**Fig. 7**), particularly in the middle and deep neurons (**Supplementary Fig. 11**). During REM, significantly fewer pyramidal cells were significantly phase-locked to gamma oscillations (REM = 10.4% versus RUN = 26.7%, $P < 0.0001$, χ^2 independent test) or modulated by both theta and gamma oscillations

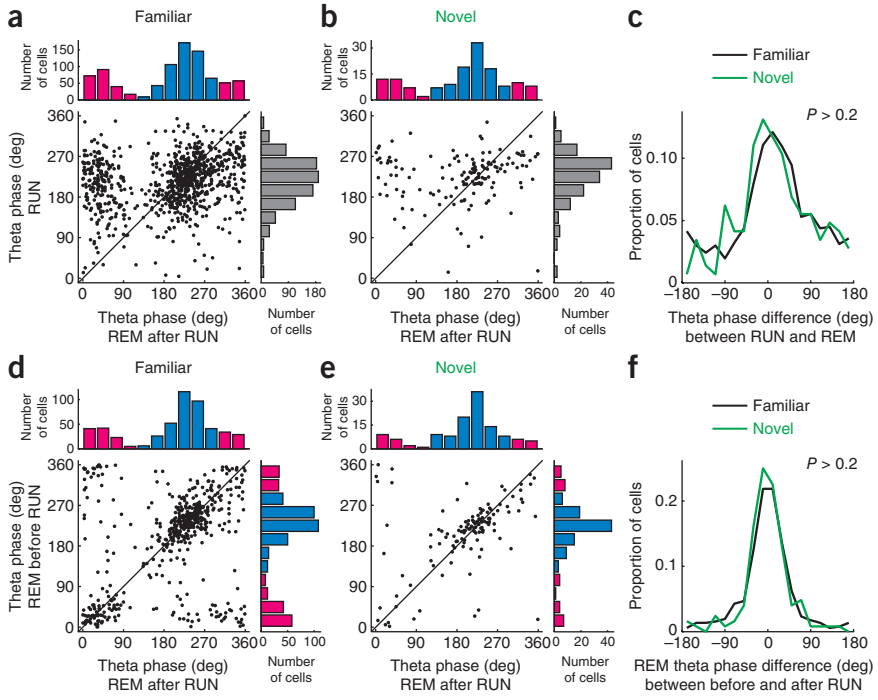

Figure 8 The theta phase of spikes during REM is not affected by novel experience. (**a**,**b**) Relationship between preferred theta phase during RUN and REM after RUN sessions in familiar (**a**) and novel (**b**) tasks. (**c**) Distribution of theta phase shifts between RUN and REM after RUN sessions. Familiar and novel tasks are shown separately. (**d**,**e**) Preferred theta phase of CA1 pyramidal neurons during REM sleeps before and after a familiar task (**d**) and a novel task (**e**). (**f**) Distribution of preferred theta phase differences between REM sleeps before and after task. Note the similar phase preference, independent of task novelty (Watson U^2 test, $P > 0.2$).

(REM = 7.2% versus RUN = 21.8%, $P < 0.0001$; **Fig. 7b,c**) than during RUN. Significantly fewer REM-shifting cells were gamma-modulated during REM sleep than during RUN ($P < 0.0001$, χ^2 independent test), whereas a comparable fraction of nonshifting cells were gamma-modulated and fired at the trough of gamma both during REM and RUN (**Fig. 7b,c**). The few gammaR pyramidal cells, which were significantly gamma phase-locked in both REM and RUN states, shifted their phase preference to the trough during REM (**Supplementary Fig. 12**). In contrast, putative CA1 interneurons maintained their gamma phase preference across behavioral states[20] (**Supplementary Fig. 13).**

Novelty does not affect theta phase preference during REM

Finally, we compared the theta phase preference of pyramidal cells during REM sleep episodes both before and after exploration of a novel ($n = 9$ sessions in 4 rats) or familiar environment ($n = 60$ sessions). We examined whether the wake-REM shift in theta phase preference of CA1 pyramidal cell spikes was experience dependent, as a previous study[31] suggested that, after exposure to a novel arm of the maze, the phase preference of novel place field cells remains the same as that observed during RUN, whereas REM sleep–related shift of phase preference emerges only after multiple experiences.

In our experiments, for the majority of CA1 pyramidal cells (that is, nonshifting cells), the preferred theta phase during REM remained similar to that during RUN, even after the familiar task (**Fig. 8a–c**). Furthermore, the distributions of theta phase difference between RUN and REM, tested after RUN sessions, were similar regardless of the familiarity of the task ($P > 0.2$, Watson U^2 test; **Fig. 8a–c**), suggesting that environmental novelty did not significantly affect preferred theta phase of spiking during REM sleep. In support of this observation, the preferred theta phases of the same neurons during REM sleep episodes before and after tasks were similar regardless of whether the task was novel or familiar (**Fig. 8d–f**).

DISCUSSION

We found subpopulations of pyramidal cells with distinct responses to inputs, spiking properties and output influence, segregated in the superficial and deep parts of CA1 stratum pyramidale. Neurons residing in different sublayers differed in multiple properties, including theta phase preference and phase-modulation strength during REM sleep, modulation by slow oscillations and sharp wave–ripples during non-REM sleep, gamma phase preference during waking state, firing rate, bursting propensity and the proportion of cells with place fields. Although the CA1 pyramidal cells have often been tacitly assumed to be a homogeneous population[15], the within-layer segregation of functional groups that we found is consistent with the relatively distinct strata of superficial and deep pyramidal cells[29].

The stratification of function in the CA1 pyramidal layer is supported by a number of anatomical and molecular observations. Several surface and channel genes show sublayer-specific expression in the pyramidal layer[24,25]. In particular, both zinc- and calbindin-containing pyramidal cells reside predominantly in the superficial layer (nearly all calbindin-immunoreactive neurons in this sublayer are zinc-positive[23]). Zinc amplifies AMPA receptor–mediated currents and suppresses NMDA receptor–mediated responses[46]. In addition, the Ca^{2+} buffer calbindin may be involved in synaptic plasticity, as long-term potentiation of Schaffer collateral synapses onto CA1 neurons and spatial learning are impaired in antisense transgenic calbindin-deficient mice[47]. Furthermore, the neurogenesis in the superficial layer occurs 1–2 d later in development than it does in the deep pyramidal cell layer[22]. Indeed, distinct subpopulations of principal neurons in each subfield (dentate gyrus, CA3 and CA1) of the hippocampus have similar gene expression profiles, distinct time windows of neurogenesis and synaptogenesis, and may form selective subcircuits[14]. Finally, neurons that project to the lateral septum are found largely in the deep CA1 sublayer[48], suggesting an output segregation of the distinct sublayers described here.

The robust correlation between the position of cells in the CA1 pyramidal layer and their physiological features may have multiple explanations. The simplest account is that intrinsic properties of pyramidal cells (morphology, distribution of ion channels, receptors, etc.) are responsible for most of the observed differences between sublayers. For example, morphological differences between the deep and superficial neurons[21,29] may differentially affect the bursting, firing rate and other biophysical properties of neurons, as has been observed in the neocortex[6,7] and the CA3 region[49]. In turn, these intrinsic features would induce the different firing patterns and phase preferences that we observed during various LFP patterns, even if all of the neurons were uniformly innervated by afferents and local interneurons. In support of this possibility, we found reliable differences in firing rates and the bursting propensities of neurons in different sublayers. During REM sleep, bursts of REM-shifting (deep) cells (<15 ms ISIs) displayed a stronger theta phase coupling than single spikes (>20 ms), and bursts and single spikes preferred opposite phases of the theta cycle.

Another possible explanation is that deep and superficial neurons are targeted by differential sets of afferents and the observed changes simply reflect the distinct influence of their upstream partners. Supporting this hypothesis, deep CA1 neurons were more effectively entrained by slow oscillation of non-REM sleep, a potential indication that these (REM shifting) neurons are more strongly driven by the entorhinal input. During theta oscillations, the CA1 region is under the competing influences of CA3 and entorhinal inputs. Again, the observed shifts of theta phase preferences of deep CA1 neurons can be explained by a stronger influence of the direct entorhinal input on these cells, given that during REM sleep EC3 principal neurons fired 10–25 ms before the REM-shifting CA1 neurons (**Supplementary Figs. 3** and **14**). Most likely, circuit and intrinsic properties interact with each other during ontogenesis so that the spatial position of neurons may correlate with both their integration into the circuitry and their intrinsic properties[12,14].

Neither intrinsic nor circuit properties alone can adequately explain the two distinct cell groups, REM-shifting and nonshifting cells, because physiological features defining the two groups are dependent on brain state. A fundamental difference between the waking state and REM sleep is the markedly reduced tonic release of several subcortical neurotransmitters, including serotonin, norepinephrine and histamine, during REM sleep[50]. Subcortical neuromodulators may distinctly affect the REM-shifting and nonshifting cells by differentially changing both their intrinsic properties and their synaptic interactions in the network in which they are embedded, thereby producing distinct changes in firing rates, bursting propensity and theta phase of spiking.

In summary, functionally distinct sublayers are present in the CA1 hippocampal region. These may serve different functions, such as melding streams of information or segregating them, depending on brain state. In the waking animal, the inputs may be integrated by the co-firing of superficial and deep neurons at the theta trough and streamlined to their joint targets. In contrast, during REM sleep, the different inputs may be kept separate, or perhaps the same inputs may address both deep and superficial neurons but can then be routed to different targets and/or at different phases of the theta cycle. Although they represent a minority, the REM-shifting deep neurons

fire bursts of spikes on the peak of theta during REM sleep and may therefore exert as powerful a downstream effect as the nonshifting, trough-preferring majority. The behavioral importance of such brain state–dependent integration and segregation of neuronal information by the CA1 region remains unknown.

METHODS

Methods and any associated references are available in the online version of the paper at http://www.nature.com/natureneuroscience/.

Note: Supplementary information is available on the Nature Neuroscience website.

ACKNOWLEDGMENTS

We thank E. Cela, S. Fujisawa, P.M. Hiche, S. Ozen, A. Sirota, E. Stark and Y. Wang for comments on the manuscript, and D. Sullivan for valuable suggestions. This work was supported by the US National Institutes of Health (NS034994, MH54671), the National Science Foundation, the J.D. McDonnell Foundation, the Uehara Memorial Foundation, the Astellas Foundation for Research on Metabolic Disorders, the Japan Society of Promotion for Sciences, and the Robert Leet and Clara Guthrie Patterson Trust.

AUTHOR CONTRIBUTIONS

K.M. and G.B. designed the experiments. K.M., K.D. and E.P. collected data. K.M. analyzed the data. K.M. and G.B. wrote the manuscript.

COMPETING FINANCIAL INTERESTS

The authors declare no competing financial interests.

Published online at http://www.nature.com/natureneuroscience/.
Reprints and permissions information is available online at http://www.nature.com/reprints/index.html.

1. Freund, T.F. & Buzsaki, G. Interneurons of the hippocampus. *Hippocampus* **6**, 347–470 (1996).
2. Markram, H. *et al.* Interneurons of the neocortical inhibitory system. *Nat. Rev. Neurosci.* **5**, 793–807 (2004).
3. Klausberger, T. & Somogyi, P. Neuronal diversity and temporal dynamics: the unity of hippocampal circuit operations. *Science* **321**, 53–57 (2008).
4. Nelson, S.B., Sugino, K. & Hempel, C.M. The problem of neuronal cell types: a physiological genomics approach. *Trends Neurosci.* **29**, 339–345 (2006).
5. Connors, B.W., Gutnick, M.J. & Prince, D.A. Electrophysiological properties of neocortical neurons *in vitro*. *J. Neurophysiol.* **48**, 1302–1320 (1982).
6. Chagnac-Amitai, Y., Luhmann, H.J. & Prince, D.A. Burst generating and regular spiking layer 5 pyramidal neurons of rat neocortex have different morphological features. *J. Comp. Neurol.* **296**, 598–613 (1990).
7. Mason, A. & Larkman, A. Correlations between morphology and electrophysiology of pyramidal neurons in slices of rat visual cortex. II. Electrophysiology. *J. Neurosci.* **10**, 1415–1428 (1990).
8. Song, S., Sjostrom, P.J., Reigl, M., Nelson, S. & Chklovskii, D.B. Highly nonrandom features of synaptic connectivity in local cortical circuits. *PLoS Biol.* **3**, e68 (2005).
9. Yoshimura, Y., Dantzker, J.L. & Callaway, E.M. Excitatory cortical neurons form fine-scale functional networks. *Nature* **433**, 868–873 (2005).
10. Varga, C., Lee, S.Y. & Soltesz, I. Target-selective GABAergic control of entorhinal cortex output. *Nat. Neurosci.* **13**, 822–824 (2010).
11. Wang, Y. *et al.* Heterogeneity in the pyramidal network of the medial prefrontal cortex. *Nat. Neurosci.* **9**, 534–542 (2006).
12. Yu, Y.C., Bultje, R.S., Wang, X. & Shi, S.H. Specific synapses develop preferentially among sister excitatory neurons in the neocortex. *Nature* **458**, 501–504 (2009).
13. Thomson, A.M., West, D.C., Wang, Y. & Bannister, A.P. Synaptic connections and small circuits involving excitatory and inhibitory neurons in layers 2–5 of adult rat and cat neocortex: triple intracellular recordings and biocytin labeling *in vitro*. *Cereb. Cortex* **12**, 936–953 (2002).
14. Deguchi, Y., Donato, F., Galimberti, I., Cabuy, E. & Caroni, P. Temporally matched subpopulations of selectively interconnected principal neurons in the hippocampus. *Nat. Neurosci.* **14**, 495–504 (2011).
15. Amaral, D. & Lavenex, P. Hippocampal Neuroanatomy. in *The Hippocampus Book* (Andersen, P., Morris, R., Amaral, D., Bliss, T.V.P. & O'Keefe, J., eds.) 37–114 (Oxford University Press, 2007).
16. Tamamaki, N. & Nojyo, Y. Preservation of topography in the connections between the subiculum, field CA1, and the entorhinal cortex in rats. *J. Comp. Neurol.* **353**, 379–390 (1995).
17. Jarsky, T., Mady, R., Kennedy, B. & Spruston, N. Distribution of bursting neurons in the CA1 region and the subiculum of the rat hippocampus. *J. Comp. Neurol.* **506**, 535–547 (2008).
18. Henriksen, E.J. *et al.* Spatial representation along the proximodistal axis of CA1. *Neuron* **68**, 127–137 (2010).
19. Golding, N.L., Kath, W.L. & Spruston, N. Dichotomy of action-potential backpropagation in CA1 pyramidal neuron dendrites. *J. Neurophysiol.* **86**, 2998–3010 (2001).
20. Senior, T.J., Huxter, J.R., Allen, K., O'Neill, J. & Csicsvari, J. Gamma oscillatory firing reveals distinct populations of pyramidal cells in the CA1 region of the hippocampus. *J. Neurosci.* **28**, 2274–2286 (2008).
21. Bannister, N.J. & Larkman, A.U. Dendritic morphology of CA1 pyramidal neurones from the rat hippocampus. I. Branching patterns. *J. Comp. Neurol.* **360**, 150–160 (1995).
22. Baimbridge, K.G., Peet, M.J., McLennan, H. & Church, J. Bursting response to current-evoked depolarization in rat CA1 pyramidal neurons is correlated with lucifer yellow dye coupling but not with the presence of calbindin-D28k. *Synapse* **7**, 269–277 (1991).
23. Slomianka, L. Neurons of origin of zinc-containing pathways and the distribution of zinc-containing boutons in the hippocampal region of the rat. *Neuroscience* **48**, 325–352 (1992).
24. Thompson, C.L. *et al.* Genomic anatomy of the hippocampus. *Neuron* **60**, 1010–1021 (2008).
25. Dong, H.W., Swanson, L.W., Chen, L., Fanselow, M.S. & Toga, A.W. Genomic-anatomic evidence for distinct functional domains in hippocampal field CA1. *Proc. Natl. Acad. Sci. USA* **106**, 11794–11799 (2009).
26. Csicsvari, J. *et al.* Massively parallel recording of unit and local field potentials with silicon-based electrodes. *J. Neurophysiol.* **90**, 1314–1323 (2003).
27. Mizuseki, K., Sirota, A., Pastalkova, E. & Buzsaki, G. Theta oscillations provide temporal windows for local circuit computation in the entorhinal-hippocampal loop. *Neuron* **64**, 267–280 (2009).
28. Ylinen, A. *et al.* Sharp wave–associated high-frequency oscillation (200 Hz) in the intact hippocampus: network and intracellular mechanisms. *J. Neurosci.* **15**, 30–46 (1995).
29. Lorente de Nó, R. Studies on the structure of the cerebral cortex. II. Continuation of the study of the ammonic system. *J. Psychol. Neurol. (Lpz)* **46**, 113–177 (1934).
30. Harris, K.D., Hirase, H., Leinekugel, X., Henze, D.A. & Buzsaki, G. Temporal interaction between single spikes and complex spike bursts in hippocampal pyramidal cells. *Neuron* **32**, 141–149 (2001).
31. Poe, G.R., Nitz, D.A., McNaughton, B.L. & Barnes, C.A. Experience-dependent phase-reversal of hippocampal neuron firing during REM sleep. *Brain Res.* **855**, 176–180 (2000).
32. Steriade, M., Nunez, A. & Amzica, F. A novel slow (<1 Hz) oscillation of neocortical neurons *in vivo*: depolarizing and hyperpolarizing components. *J. Neurosci.* **13**, 3252–3265 (1993).
33. Isomura, Y. *et al.* Integration and segregation of activity in entorhinal-hippocampal subregions by neocortical slow oscillations. *Neuron* **52**, 871–882 (2006).
34. Harris, K.D. *et al.* Spike train dynamics predicts theta-related phase precession in hippocampal pyramidal cells. *Nature* **417**, 738–741 (2002).
35. Mehta, M.R., Lee, A.K. & Wilson, M.A. Role of experience and oscillations in transforming a rate code into a temporal code. *Nature* **417**, 741–746 (2002).
36. O'Keefe, J. & Dostrovsky, J. The hippocampus as a spatial map. Preliminary evidence from unit activity in the freely-moving rat. *Brain Res.* **34**, 171–175 (1971).
37. Muller, R.U. & Kubie, J.L. The firing of hippocampal place cells predicts the future position of freely moving rats. *J. Neurosci.* **9**, 4101–4110 (1989).
38. Hafting, T., Fyhn, M., Bonnevie, T., Moser, M.B. & Moser, E.I. Hippocampus-independent phase precession in entorhinal grid cells. *Nature* **453**, 1248–1252 (2008).
39. Skaggs, W.E., McNaughton, B.L., Gothard, K.M. & Markus, E.J. An information-theoretic approach to deciphering the hippocampal code. in *Advances in Neural Information Processing Systems, vol. 5* (Hanson, S.J., Cowan, J.D. & Giles C.L., eds.) 1030–1037 (Morgan Kaufmann, 1993).
40. Skaggs, W.E., McNaughton, B.L., Wilson, M.A. & Barnes, C.A. Theta phase precession in hippocampal neuronal populations and the compression of temporal sequences. *Hippocampus* **6**, 149–172 (1996).
41. Markus, E.J., Barnes, C.A., McNaughton, B.L., Gladden, V.L. & Skaggs, W.E. Spatial information content and reliability of hippocampal CA1 neurons: effects of visual input. *Hippocampus* **4**, 410–421 (1994).
42. O'Keefe, J. & Recce, M.L. Phase relationship between hippocampal place units and the EEG theta rhythm. *Hippocampus* **3**, 317–330 (1993).
43. Bragin, A. *et al.* Gamma (40–100 Hz) oscillation in the hippocampus of the behaving rat. *J. Neurosci.* **15**, 47–60 (1995).
44. Whittington, M.A., Traub, R.D. & Jefferys, J.G. Synchronized oscillations in interneuron networks driven by metabotropic glutamate receptor activation. *Nature* **373**, 612–615 (1995).
45. Csicsvari, J., Jamieson, B., Wise, K.D. & Buzsaki, G. Mechanisms of gamma oscillations in the hippocampus of the behaving rat. *Neuron* **37**, 311–322 (2003).
46. Peters, S., Koh, J. & Choi, D.W. Zinc selectively blocks the action of *N*-methyl-D-aspartate on cortical neurons. *Science* **236**, 589–593 (1987).
47. Molinari, S. *et al.* Deficits in memory and hippocampal long-term potentiation in mice with reduced calbindin D28K expression. *Proc. Natl. Acad. Sci. USA* **93**, 8028–8033 (1996).
48. Sørensen, J.C., Tonder, N. & Slomianka, L. Zinc-positive afferents to the rat septum originate from distinct subpopulations of zinc-containing neurons in the hippocampal areas and layers. A combined fluoro-gold tracing and histochemical study. *Anat. Embryol. (Berl.)* **188**, 107–115 (1993).
49. Bilkey, D.K. & Schwartzkroin, P.A. Variation in electrophysiology and morphology of hippocampal CA3 pyramidal cells. *Brain Res.* **514**, 77–83 (1990).
50. Pace-Schott, E.F. & Hobson, J.A. The neurobiology of sleep: genetics, cellular physiology and subcortical networks. *Nat. Rev. Neurosci.* **3**, 591–605 (2002).

ONLINE METHODS

Animals and surgery. Ten male Long-Evans rats (250–400 g) were implanted with a 4- or 8-shank silicon probe in the right dorsal hippocampus under isoflurane anesthesia (1–1.5%) and recorded from dorsal CA1 pyramidal layers. In four of the rats, another 4-shank silicon probe was also implanted in the right dorsocaudal medial entorhinal cortex[27]. The silicon probes were attached to micromanipulators and moved slowly to the target. Each shank had eight recording sites (160 μm^2 each site, 1–3-MΩ impedance) and inter-shank distance was 200 µm. Recordings sites were staggered to provide a two-dimensional arrangement (20-µm vertical separation). The entorhinal cortex probe was positioned so that the different shanks recorded from different layers[27]. Histological and electrophysiological localization of recording sites in the entorhinal cortex was described previously[27]. Two stainless steel screws inserted above the cerebellum were used as indifferent and ground electrodes during recordings. All protocols were approved by the Institutional Animal Care and Use Committee of Rutgers University.

Behavioral testing. Physiological signals during waking were recorded during six different tasks: a task on the linear track (250 cm × 7 cm), a task on the open field (180 cm × 180 cm, or 120 cm × 120 cm), a wheel running task, an alternation task in the T maze (100 cm × 120 cm) with wheel running delay (described previously[27]), an elevated plus maze (100 cm × 100 cm) in which the rats were motivated to run to the ends of four corridors, where water was given every 30 s, and a zig-zag maze (100 cm × 200 cm) with 11 corridors, in which the rats learned to run back and forth between two water cups placed in the first and last corridors. Theta periods from all maze behaviors were lumped together as RUN. The task was regarded as being novel when the animal performed it for the first time and familiar after at least three testing sessions.

Data collection and cell-type classification. Detailed information about the recording system and spike sorting has been described[27]. Briefly, signals were amplified (1,000×), bandpass-filtered (1 Hz to 5 kHz) and acquired continuously at 20 kHz. LFP was down-sampled to 1,250 Hz for additional analysis. Spike sorting was performed by KlustaKwik (http://klustakwik.sourceforge.net/), followed by manual adjustment of the clusters (Klusters software package, http://klusters.sourceforge.net/). CA1 pyramidal cells and interneurons were separated as described[27]. Cell-type classification of entorhinal cortical neurons was described previously[27]. A total of 3,541 (CA1), 491 (EC2), 576 (EC3) and 559 (EC5) principal neurons and 468 (CA1), 85 (EC2), 217 (EC3) and 94 (EC5) interneurons were identified and used for analyses. Median isolation distances[30], reflecting the quality of cluster isolation, were similar across the deep, middle and superficial CA1 pyramidal cells (28.7, 28.3 and 28.7, respectively; $P > 0.13$, Wilcoxon rank sum test).

Detection of brain states. Theta periods during task performance (RUN), REM epochs and slow-wave sleep (SWS) were detected using the ratio of the power in theta band (5–11 Hz) to delta band (1–4 Hz) of LFP, followed by manual adjustment with the aid of visual inspection of whitened power spectra and the raw traces[27]. REM periods were cross-validated with experimenter notes taken while observing theta activity on-line in sleep session and verifying that the rat was sleeping.

To detect gamma epochs, we used a recording site with the highest ripple power in a given shank. LFPs were band-pass filtered (30–80 Hz) and the power (r.m.s.) of the filtered signal was calculated in 80-ms time windows. Gamma phase of spiking was computed in gamma oscillatory periods. Gamma oscillatory periods were defined as epochs with gamma power larger than the 85 percentile of gamma power. If the gap between epochs was shorter than 30 ms, these flanking epochs were combined, generating a single epoch. Epochs less than 40 ms were discarded. The detected gamma periods represented 19.8 ± 3.4% of RUN, 13.2 ± 3.3% of REM sleep, 12.8 ± 2.0% of SWS and 17.9 ± 2.8% of awake nontheta epochs (mean ± s.d.).

To detect ripple events, LFPs in CA1 pyramidal layer during nontheta periods were band-pass filtered (140–230 Hz), and the power (r.m.s.) was calculated in 17-ms time windows. Ripple epochs were defined as periods during which ripple power was continuously greater than mean + 3 s.d., and peak of power in the periods were greater than mean + 7 s.d. Events shorter than 15 ms were discarded.

DOWN-UP transitions in the entorhinal cortex were detected by using spiking activity of entorhinal cortex neuron population during slow wave sleep. All the simultaneously recorded single entorhinal cortex neurons were combined as a multi-unit activity (MUA), and smoothed with a Gaussian kernel (s.d. = 10 ms, kernel size = 60 ms). Upstate onsets were detected if the following criteria were all fulfilled. First, the smoothed MUA exceeded the upstate threshold, defined as the geometric mean of all nonzero MUA. Second, the mean MUA in a 150-ms window before the onset of the candidate event was below the downstate threshold, which was defined as 0.16 times the upstate threshold. Third, the mean MUA in both 100-ms and 200-ms window after the onset candidate was above the upstate threshold. The frequency of the detected DOWN-UP transitions was 0.45 ± 0.14 Hz (mean ± s.d.). To compare the magnitude of DOWN-UP modulation between cell groups, we computed the modulation index for each neuron.

$$\text{Modulation Index} = \frac{N_{\text{spikesUP}} - N_{\text{spikesDOWN}}}{N_{\text{spikesUP}} + N_{\text{spikesDOWN}}}$$

where $N_{\text{spikesDOWN}}$ is the number of spikes from −200 to 0 ms, and N_{spikesUP} is the number of spikes from 0 to 200 ms (time 0 = DOWN-UP transition). One-way ANOVA or *t* test was used to test the significance.

Localization of neuronal somata in the CA1 pyramidal layer. For each silicon probe shank, one recording site was chosen first and used to detect ripple epochs as described above. LFP recorded from each recording site was band-pass filtered (140–230 Hz) and the power (r.m.s.) was calculated in 17-ms time windows. The site with the largest mean power during ripple epochs, reflecting the middle of the pyramidal layer[28], was determined for each shank for each session and served as the reference depth. The site with the largest average spike amplitude for each unit was regarded as the approximate location of the cell body[26]. The error of cell body assignment was 20 µm, due to the limitation of the vertical distance between recording sites.

Theta and gamma phase modulation. Three methods were used to determine the phase of band-pass filtered theta (5–11 Hz) or gamma (30–80 Hz) waves $y(t)$[27]. First, instantaneous phase was derived from Hilbert transform of $y(t)$. Second, peaks (0°) of filtered waves were identified as the positive to negative zero crossings of the derivative dy/dt, and phase was linearly interpolated between the peaks. Third, troughs (180°) of filtered waves were identified as the negative-to-positive zero crossings of the derivative dy/dt, and phase was linearly interpolated between the troughs. A phase value was assigned to each action potential using linear interpolation. Peaks are at 0° and 360° and troughs at 180° throughout the paper. The results obtained by these three methods were consistent and the peak method was used for both theta and gamma phases. The mean direction and mean resultant length of the phases of a given neuron's spikes were taken as the preferred phase and modulation depth of that neuron, respectively. For the preferred phase and modulation depth, only neurons that were significantly modulated by the oscillations are shown. For the circular statistics of theta phase of single cells, only neurons with at least 50 spikes during theta epochs (RUN or REM) were used, and $P < 0.01$ (Rayleigh test) was used to define significantly theta-modulated neurons. For gamma modulation of single cells, only neurons with at least 20 spikes during gamma oscillatory periods in relevant brain state (RUN, REM, SWS or awake nontheta) were used and $P < 0.05$ (Rayleigh test) was used to define significantly gamma-modulated neurons[20]. To avoid gamma phase variability as a function of depth[45], the recording site with the largest ripple power (that is, the middle of the CA1 pyramidal layer) for each probe shank was used for detecting gamma phase.

ISI analysis. Burst index was defined as the ratio of bursting spikes to all spikes. A bursting spike was defined as a spike associated with ISI at least either before or after that spike smaller than 6 ms. To compute the circular statistics of theta phase at different ISIs, we first sorted the spikes of a neuron according to their ISIs. A spike associated with an ISI either before or after that spike less than 6, 8, 10, 15 ms was sorted into <6-ms, <8-ms, <10-ms or <15-ms ISI groups, allowing less stringent groups to redundantly contain spikes in more stringent groups. Therefore, the <15-ms ISI group contains the <6-ms, <8-ms and <10-ms groups. A spike associated with ISIs both before and after that spike larger than 20, 30, 50 or 100 ms was sorted into >20-ms, >30-ms, >50-ms or >100-ms ISI groups.

Therefore, the >20-ms ISI group contains the >30-ms, >50-ms and >100-ms groups. The preferred phase, modulation depth and *P* value of Rayleigh test were calculated for each ISI group of each neuron. If the number of spikes from a given cell in a given ISI group was greater than 50 and associated *P* value was less than 0.01, the cell was regarded as being significantly theta-modulated in that ISI group.

Spatial tuning of spiking activity. Data recorded on the open field (180 cm × 180 cm) and linear track (250 cm) were used for the analysis of spatial tuning of spiking activity. Only the data during theta epochs were used. Position of the animal was estimated by recording LEDs on the head stage at 30 Hz. For the linear track, the positions were projected onto the track axis. The position and spiking data were sorted into 5 cm × 5 cm (open field) or 5 cm (linear track) bins, generating the raw maps of spike number and occupancy. For the linear track, spatial representation (rate map, number of place fields, spatial information[39], spatial coherence[37], stability[41] and phase precession[42]) was analyzed for each direction separately. A raw rate map was constructed by dividing a raw spike map by a raw occupancy map and then used to compute spatial coherence[27,37,38]. Peak firing rate, number of place fields, stability[41] and spatial information[39] were computed from the smoothed rate map. To construct smoothed rate map for open field, we used an adaptive smoothing[18,40]. The firing rate at each bin was estimated by expanding a circle around the bin until

$$N_{\text{spikes}} > \frac{\alpha}{N_{\text{occ}}^2 r^2}$$

where N_{occ} is the occupancy time (in seconds) in the circle, N_{spikes} is the number of spikes emitted in the circle, r is the radius of the circle in bins and α is a scaling parameter, set at 40,000. The firing rate at that bin was then set to $N_{\text{spikes}}/N_{\text{occ}}$.

For the linear track, a Gaussian kernel (s.d. = 5 cm) was applied for both raw maps of spike and occupancy, then the smoothed rate map was constructed by dividing the smoothed spike map by the smoothed occupancy map. Area at 0–25 cm (starting point) was excluded from the analysis to exclude the effect of behavioral variability. A place field was defined as a contiguous region of at least 225 cm^2 (nine bins) for the open field and 15 cm (three bins) for the linear track where the firing rate was above 10% of the peak rate in the maze and the peak firing rate of the area was >2 Hz. Using a threshold of 20% of the peak rate gave similar results (data not shown). The results using rate threshold of 0.5, 1, 2 and 4 Hz for the peak firing rate of place field were essentially similar and are shown in **Supplementary Figure 8**. Place map stability[41] was defined by the bin-by-bin correlation coefficient between the firing rate maps of the first and second half of the recording session. Theta phase-position correlation and mean theta phase in place field were calculated as described previously[27,38].

Detection of phasic REM. REM epochs were detected as described above. To detect phasic REM epochs, we first band-pass filtered (5–12 Hz) LFP traces during REM epochs, yielding $y(t)$. The amplitudes of theta oscillations were derived from Hilbert transform of $y(t)$, and peaks of theta oscillations were detected as the positive-to-negative zero crossings of the derivative dy/dt. Interpeak intervals were smoothed using an 11-sample rectangular kernel. Candidate epochs were detected if smoothed interpeak intervals were shorter than the 10th percentile of smoothed interpeak intervals. The candidate epochs were identified as phasic REM epochs if the following criteria were all fulfilled. First, the duration of an epoch was longer than 900 ms. Second, the minimum of smoothed interpeak intervals during an epoch was shorter than the 5th percentile of smoothed interspike intervals. Third, the mean amplitude of theta oscillations during an epoch was larger than the mean amplitude of theta oscillations during the entire REM sleep. A total of 5,844 s (3.68 % of REM sleep episodes) was identified as phasic REM epochs.

Firing rate correlations between left and right journeys on the linear track. First, smoothed firing rate maps were constructed as described above. Firing rate correlations (Pearson product moment correlation coefficient) between left versus right journeys on the linear track were computed in two different ways. First, bin-by-bin firing rate correlation between the left and right journeys was calculated (**Supplementary Fig. 10i**). This correlation provides information about the strength of rate-position relationship of a neuron, when position is referenced to distant (room) cues. Second, the firing rate map during left journeys was reversed, and bin-by-bin firing rate correlation between the right journeys and reversed left journeys was calculated (**Supplementary Fig. 10j**). This correlation provides information about the strength of rate-position relationship of a neuron, when position is referenced to the start (or goal) position.

doi:10.1038/nn.2894